Wavelet analysis of properties of marine boundary layer mesoscale cells observed from AMSR-E

Xiaoli Zhou[1,2,3], Christopher S. Bretherton[1], Ryan Eastman[1], Isabel L. McCoy[1,4], Robert Wood[1]

[1]Department of Atmospheric Sciences, University of Washington, Seattle, Washington, USA

[2]*now at NOAA Chemical Sciences Laboratory (CSL), Boulder, Colorado, USA

[3]*now at Cooperative Institute for Research in Environmental Sciences (CIRES), University of Colorado, Boulder, Colorado, USA

[4]Rosenstiel School of Marine and Atmospheric Sciences, University of Miami, Miami, Florida, USA

Abstract

Marine boundary layer clouds tend to organize into closed or open mesoscale cellular convection (MCC). Here, two-dimensional wavelet analysis is applied for the first time to passive microwave retrievals of cloud water path (CWP), water vapor path (WVP), and rain rate from AMSR-E in 2008 over the Northeast and Southeast Pacific, and the Southeast Atlantic subtropical stratocumulus to cumulus transition regions. The (co-)variability between CWP, WVP, and rain rate in 160x160 km^2 analysis boxes is partitioned between four mesoscale wavelength octaves (20, 40, 80, and 160 km). The cell scale is identified as the wavelength of the peak CWP variance. Together with a machine-learning classification of cell type, this allows the statistical characteristics of open and closed MCC of various scales, and its relation to WVP, rain rate and potential environmental controlling factors to be analyzed across a very large set of cases.

The results show that the cell wavelength is most commonly 40-80 km. Cell-scale CWP perturbations are good predictors of the WVP and rain rate perturbations. A universal cubic dependence of rain rate on CWP is found in closed and open cells of all scales. This suggests that aerosol control on precipitation susceptibility is not as important for open cell formation as are processes that cause increases in cloud water. For cells larger than 20 km, there is no obvious dependence of cell scale on the environmental controlling factors tested, suggesting that the cell scale may depend more on its historical evolution than the current environmental conditions.

Key points:

1 Two-dimensional wavelet analysis is applied for the first time to a full year of passive microwave retrievals from AMSR-E.

2 Cell-scale CWP perturbations are good predictors of the WVP and rain rate perturbations, similar between open and closed cells.

3 A universal cubic dependence of rain rate on CWP is found in closed and open cells of all scales.

1. Introduction

Marine boundary layer clouds over the colder regions of the ocean often organize into closed or open mesoscale cellular convection (MCC) with cell sizes between 10-100 km, modulating cloud water path, precipitation, and albedo (Agee et al., 1973). MCC is associated with significant mesoscale variations of moisture (~10% relative humidity perturbation), temperature, and winds (Rothermel and Agee, 1980). MCC-like patterns can be simulated in large-eddy simulations, weather and climate models with horizontal grid resolutions of O(10 km) or less (e. g. Boutle and Abel, 2012). To evaluate their skill requires good documentation and understanding of MCC cloud morphology and scale, of co-variability between observable quantities within closed and open cells, and of the sensitivity of closed and open MCC to potential environmental controlling factors across different boundary-layer cloud regions.

There is a 50-year history of MCC observations from in-situ and satellite measurements that has advanced our understanding and provided local data that has been used for model comparisons. MCC was first observed by the first weather satellites in the early 1960s (Agee, 1984). MCC covers extensive regions over the eastern subtropical oceans (Wood & Hartmann, 2006; Muhlbauer et al., 2014), with closed cells forming near the coast and open cells occurring towards the warm oceans (Atkinson and Zhang, 1996; Muhlbauer et al., 2014). Closed and open cells can be considered as different stages of the stratocumulus to cumulus transition (Wood, 2012), which is often associated with the advection of clouds over a warmer ocean surface (Bretherton & Wyant, 1997; Sandu & Stevens, 2011), or with the passage of cyclones and cold air outbreaks (Field et al., 2014; Yamaguchi and Feingold, 2015; Fletcher et al., 2016; Abel et al., 2017; McCoy et al., 2017). Eastman et al., (2021) finds that increased wind speed favors open cells. Previous idealized model and observational studies have suggested that precipitation differs significantly between closed and open cells and can be a microphysical trigger of transition between the two (Sharon et al., 2006; Stevens et al., 2005;

Wang et al., 2009; Xue et al., 2008; Savic-Jovcic and Stevens, 2008; Goren and Rosenfeld, 2012; Berner et al., 2013; Abel et al., 2020).

Global statistical analyses of MCC useful for comparing with models and theories are scarce. Agee et al. (1973) published the first global map of open and closed cell occurrences estimated from positions of warm and cold ocean currents, respectively. With the advent of neural network algorithms and their easy application to satellite data, this qualitiative MCC climatology has been quantified and statistically connected to environmental controls (Wood and Hartmann, 2006; Muhlbauer et al. 2014; McCoy et al. 2017). Additionally, Wood and Hartmann (2006) found that typical MCC cell sizes increase with boundary layer depth, maintaining an approximate aspect ratio of 40:1.

One underexploited tool to probe MCC is passive microwave remote sensing of cloud water path (CWP), water vapor path (WVP) and precipitation. Zhou and Bretherton (2019b) used ground-based microwave radiometer (MWR) observations from the ARM Eastern North Atlantic (ENA) size at Graciosa Island to analyze correlations between CWP and WVP and test predictions of a humidity self-aggregation mechanism of MCC proposed by Zhou and Bretherton (2019a). The ground-based MWR measurements are useful for case studies, but they suffer from sensor wetting during and after precipitation (Turner et al., 2007) and are limited to only a few locations.

In this study, we take a wider satellite-based view of the mesoscale variability within closed and open MCC using two instruments on NASA's Aqua satellite. The backbone of our analysis is the Advanced Microwave Scanning Radiometer for Earth Observing System (AMSR-E, Wentz and Meissner, 2004), used to derive CWP, WVP, and rain rate. This is coupled with cell type classifications from a machine learning algorithm using visible satellite imagery from the NASA Moderate Resolution Imaging Spectroradiometer (MODIS, King et al., 1992). These datasets are discussed in Section 2. In Section 3, a two-dimensional wavelet analysis (e. g. Lau et al., 1995; Torrence and Campo, 1998) of CWP is used to identify a dominant local time and space dependent MCC scale where detectable. The analysis is also used to partition the co-variability between CWP and WVP between scales. It is easily statistically aggregated across many satellite images in subtropical stratocumulus regimes and their downstream transition to cumulus. In Section 4, we show the dependence of MCC properties on cellular scale. Section 5 discusses the relationship between CWP and rain rate. Environmental controls on MCC scale and type are analyzed in Section 6. Section 7 synthesizes results of Sections 4 and 5 into a mesoscale cell composite. Section 8 concludes with a discussion and summary.

2. Data

2.1. Regions

Three subtropical stratocumulus and downstream cloudiness transition regions selected by Eastman and Wood (2016) are used in this study, the Northeast (NE) Pacific (15º-30ºN, 155º-115ºW), the Southeast (SE) Pacific (30º-5ºS, 105º-70ºW), and the Southeast (SE) Atlantic (30º-5ºS, 15ºW-15ºE). We leave out the eastern Indian Ocean included in Eastman and Wood (2016) because it has less stratocumulus coverage than the other three regions. All available data from 2008 are used.

2.2. AMSR-E

CWP and WVP in this study are sourced respectively from the columnar cloud liquid water and columnar water vapor in the AMSR-E Aqua L2B global swath ocean products derived from the Wentz Algorithm (version 2, Wentz and Meissner, 2004). The Aqua satellite is part of the A-Train satellite constellation that crosses the equator at 0130 and 1330 local times. The AMSR-E has a swath width of 1445 km. The retrievals are provided on a non-uniform grid within the swath with pixel resolution of ~10 km at center-track, but the footprints of some of the sampled wavelengths are at a coarser resolution. The CWP retrieval relies heavily on the 37 GHz channel with a 14 x 8 km footprint, and the WVP retrieval relies mostly on the 19 GHz channel with a 27 x 16 km footprint. This means that WVP can only be resolved at scales larger than ~ 20 km. Estimated root mean square (RMS) error for the CWP and WVP retrievals are 0.017 mm and 0.57 mm respectively (Wentz and Meissner, 2004).

Rain can complicate microwave retrieval techniques by requiring a priori partitioning of total water into cloud and rain components. Seethala and Horváth (2010) found a systematic low bias in Wentz CWP retrievals above 0.18 mm (a CWP threshold used to indicate rain) due to the algorithm assigning to large a fraction of the liquid water content of thicker nonprecipitating clouds to rain; they estimated this low bias increases with CWP and reaches 30% for CWP of 0.35 mm. Since most the clouds used in our MCC analysis clouds have CWP below 0.18 mm (Section 4), this possible low bias in CWP is not expected to alter the results of this study.

For calculating MCC cell scale and other wavelet-based statistics, AMSR-E pixels are divided into ‘boxes’ of 16 x 16 grid points (~160 x 160 km^2 near nadir). This size allows two-dimensional wavelet decompositions across four wavelength octaves (see Section 3) to capture the mesoscale variability within each box. To ensure a robust scale estimate from wavelet analysis, which requires

nearly evenly distributed points in the sample boxes, the first 99 pixels from the right of each arcing swath are excluded from the analysis, as they are severely distorted.

2.3 Mesoscale Cellular Convection Identification

The warm MCC cloud morphology identification dataset used in this study is derived from the application of the neural net (NN) defined in Wood and Hartmann (2006) to a full year of satellite-derived cloud water path (CWP) in 2008. CWP is estimated based on Collection 6 Level 2 daytime marine cloud retrievals (cloud optical depth and effective radius) at 1 km (nadir) resolution from MODIS on the Aqua satellite (Wood and Hartmann, 2006). MODIS CWP is divided into scenes of 256 x 256 km^2 in size oversampled by 128 km in each direction. Each overlapping scene is classified into one of the three morphological types: closed MCC, open MCC, and cellular but disorganized clouds. The corresponding cloud types are placed at the center of each overlapping scene with 128 km resolution. Details of the cloud type classification are given by Wood and Hartmann (2006).

To adopt this cloud identification dataset to our analysis, we re-grid the $(128\ km)^2$ MCC data onto AMSR-E CWP resolution (~10 km) using nearest-neighbor interpolation. The re-gridded MCC cloud types are then regrouped to the 16 x 16 AMSR-E grid-box scenes . If over 50% of the pixels in an AMSR-E scene have been assigned the same MCC cloud type, the scene is considered to have that cloud type, otherwise it is classified as “Mixed pattern MCC”. Using this definition, of the 403904 collected scenes, 7% are closed cell cases, 8% are open cell cases, 30% are disorganized cases, and the rest are mixed pattern MCC cases. A stricter 90% classification threshold of like-classified pixels in a scene reduces the number of samples of each MCC cloud type but has little effect upon the derived statistics.

2.3. Light Rain Rate Retrieval

The light rain rate in this study is retrieved from AMSR-E 89-GHz brightness temperature T_b following Eastman et al. (2019). This has advantages over the AMSR-E Aqua level-2B instantaneous surface rain product (AE_Rain; Kummerow et al., 2015), which is based on the same two frequencies (37 GHz and 19 GHz) used to derive CWP and WVP. The 89 GHz channel gives an independent retrieval that is more sensitive to drizzle, has a smaller footprint, and better matches high-resolution CloudSat retrievals (Eastman et al., 2019). The rain rate data are spatially interpolated and grouped into the same 16 x 16 grid-box scenes used for CWP and WVP.

2.4. Meteorological Control Metrics

Four environmental variables are examined in this study: sea surface temperature (SST), 10-m wind speed, estimated inversion strength (EIS), and planetary boundary layer (PBL) depth. SST and 10-m wind speed are taken from the ERA-Interim reanalysis on a 1º x 1º latitude-longitude grid (Dee et al., 2011). EIS is calculated following Wood and Bretherton (2006) using fields from ERA-Interim. Following Eastman et al. (2017), the PBL depth is estimated from the difference between the SST and cloud top temperature (CTT) along with a parametrized lapse rate (Wood and Bretherton, 2004). Here CTT is sourced from the MODIS Aqua joint CTT histograms on the 1ºx1º L3 grid (King et al., 2003). The CTT is corrected for partial cloudiness when cloud amount is below 90% (Eastman et al., 2017). PBL depths are only estimated when cloud amount is greater than 30%. All data are interpolated to match the AMSR-E data grid and regrouped into 16 x 16 grid boxes.

3. **Mesoscale decomposition using wavelet analysis**

We apply a 2D discrete wavelet transform (DWT) as a band-pass filter bank in space to filter out synoptic-scale variability of CWP, WVP, and rain rate, and to segregate the gridded data into mesoscale wavelet octaves.

3.1 Key aspects of 2D DWT

This section presents key aspects of the 2D DWT for our application. The wavelet transform is based on an octave band decomposition of the space-wavelength plane, and hence is a powerful mathematical tool for analysis of multi-scale features (Kumar and Foufoula-Georgiou, 1997). We use a 2D multilevel DWT, mathematically described in Mallat (1989a&b), Daubechies (1988, 1992), and Meyer (1992). This partitions a spatial field into 'details' at multiple 'levels' (scale octaves) p = 1, ..., P, by successive application of wavelet transforms of levels 1, 2, …P. The maximum level P is chosen by the user based on the largest scales of interest for the analysis. For each 2^p x 2^p block of grid points, the level-p wavelet transform computes three 'details' (representing variability in the x, y, and diagonal direction respectively) and an 'average' representing variability at coarser scales, which can iteratively be decomposed using wavelet transforms of levels p + 1 and higher. After applying this process successively to levels 1 to P, the level P averages and the details from levels 1 to P can be concatenated into a wavelet-transformed matrix with the same size as the original data.

It is straightforward to invert the 2D wavelet transform to recreate the original field from this matrix. The field can be filtered to a particular scale level p by zeroing out all of the coefficients

of the wavelet-transformed matrix except for the details of level p; the same principle can be applied to band-pass filter the field to a range of octave scales p_1 to p_2. The variance of the field can also be wavelet-decomposed by scale level using the squares of the details. This decomposition is approximately spatially local, so that within an individual 2^P x 2^P block of grid points, the variance at scale $p < P$ is the squared sum of the level-p details in that block.

Different choices of wavelet allow trade-offs between two desirable characteristics: 'locality' (keeping sharp discontinuities localized to details in just a few spatial blocks, and minimizing artifacts near the edge of the spatial domain) and 'spectral accuracy' (making the details into more accurate octave band-pass filters of the original spatial field with less spectral leakage). Spectral accuracy ensures details are less contaminated by strong broad scale gradients prominent in fields such as WVP. We use Daubechies' orthogonal wavelet (Daubechies, 1988; hereafter *dbN* where the index number *N* refers to the number of coefficients) as our analyzing mother wavelet. The larger the *N*, the closer the spectral power is to a perfect octave band-pass response and the larger the number of adjacent grid-points used. The *db*3 wavelet is adopted in this study since it is a fairly accurate band-pass filter, yet sharp enough to capture abrupt variations.

3.2 Application of 2D DWT to the satellite microwave dataset

Specifically, we apply a 2D DWT to segregate the gridded microwave-derived CWP, WVP and rain rate into $P = 4$ mesoscale wavelength octaves. Given the nominal 10 km grid scale of this data, these octaves correspond to characteristic wavelengths of 20, 40, 80, and 160 km. Since the CWP data has an 14 km x 8 km footprint, it is under-resolved at the 10 km pixel scale of our gridded AMSR-E data, so variability in the 20 km wavelength octave may be underestimated. For WVP (27 km x 16 km footprint), variability in the 20 km octave will be primarily unphysical noise, and variability in the 40 km octave may be underestimated. Rain rate has a footprint smaller than the pixel scale and does not suffer from these issues. The wavelet coefficients in a given 16 x 16 grid box also depend on the data in neighboring grid boxes. For each 16 x 16 grid box, there are 256 wavelet coefficients: $3 \cdot (2^3)^2$ level 1 (20 km wavelength) details, $3 \cdot (2^2)^2$ level 2 (40 km wavelength) details, $3 \cdot 2^2$ level 3 (80 km wavelength) details, 3 level 4 (160 km wavelength) details, and one level 4 average. We use a 2D inverse wavelet transform to obtain the local fluctuations of these fields at the corresponding four scales or combinations thereof; again this involves wavelet coefficients from neighboring boxes as well as the box of interest.

An example of wavelet decomposition of CWP can be seen in Figs. 1 and 2. Figure 1 shows a 10ºx10º Aqua MODIS scene over the SE Pacific on 11 August 2008 that includes various cloud types and scales. A 16 x 16 AMSR-E grid box (~160 km x160 km) in a region of closed cells is highlighted in red. Fig. 2 shows the corresponding AMSR-E CWP in this area (Fig. 2a) and the wavelet-reconstructed CWP contributions from level 1 (20 km wavelength) up to level 4 (160 km wavelength) (Figs. 2b-e).

Recall that the wavelet decomposition approximately partitions the variance of a field into contributions from each of the analyzed wavelength octaves. In each 16 x16 box, we calculate the CWP variances of the four wavelength octaves, and we identify the cell scale as the wavelength of the peak variance in this spectrum. In the highlighted box, CWP variance is the largest at level 3 (80 km wavelength), hence the cloud scale in this box is determined as 80 km, consistent with visual inspection of Fig. 2a. Based on the RMS sampling errors cited in Sect. 2.2, only a CWP standard deviation exceeding 0.017 mm can be detected above the background noise of the microwave retrieval for MCC cells, so only 16 x16 blocks meeting this criterion are retained in the study. This leaves 23,866 closed cell cases and 26,315 open cell cases, which are the majority of the available closed and open scenes as we can get from the MCC classifier.

Figures 3a-3c shows the CWP, WVP, and rain rate over the same region as in the MODIS scene of Fig. 1. Clouds with various scales as seen on the MODIS image are fairly well detected by AMSR-E CWP, although it is difficult to distinguish the boundary between closed and open cells that is obvious in the MODIS scene. The thicker clouds (high CWP) to the southwest and the center of the region are associated with more higher rain rate than their northeast counterpart (Fig. 3c). Fig. 3d indicates that the southwest region has patches of open cells with cell scales (wavelengths) of 20 km or 40 km. The center region is filled with patches of closed cells with scales ranging from 20-80 km. The north and northeast regions contain thin clouds with predominantly closed-cell organization as identified by the MCC classification algorithm. The CWP variability in this region is only barely detectable by AMSR-E (Fig. 3a), even though it is obvious in the MODIS visible image (Fig. 1). Sometimes, cells we would subjectively classify as closed cells based on their appearance are classified as open cells by the automated, CWP based algorithm. These instances may be occurring when clouds are observed shortly after their transitions from closed to open cells, a difficulty in applying discrete identifications to a non-discrete system. Hereafter, we focus on closed and open cell cases only, for which the classifications are the most reliable.

Boxes labeled with 160 km scale should be interpreted with caution, since they can also include cells with wavelengths greater than 160 km and transitions between closed cells and open cells (or clear sky) that are falsely identified by the NN algorithm as large closed cells. For instance, in the 10º x 10º scene presented in Figs. 1 and 3, 160 km scale MCCs are detected in the northeast region (around 84ºW, 14ºS; 81ºW, 10ºS; 80ºW, 16ºS) where there are mesoscale patches of clear sky embedded in the closed cell region.

There is a latitudinal gradient of column moisture with the more tropical northern region ~8 mm moister than the south (Fig. 3b). This likely comes primarily from the free troposphere, with some contribution from gradients in boundary-layer depth and humidity. The mesoscale variability of WVP is more clearly seen from its fluctuation in Fig. 3e reconstructed from an inverse wavelet transform of detail levels 1-4, which filters out the large scale variability with scales greater than 160 km. The reconstructed fluctuation of WVP correlates fairly well with that of CWP (Figs. 3d and 3f), and with that of rain rate when it is present (Fig. 3f), except that there is considerable WVP variability at 160 km and WVP noise at 20 km in the northeast region despite the weak cellularity in CWP.

The same example box shown in red in Figs. 1 and 2 is indicated in white in Fig. 3d. Figs. 3g-3i show the reconstructed CWP, WVP, and rain rate fluctuations in and around this box of 16 x16 AMSR-E pixels. Combining the four wavelength octaves reliably reproduces the multi-scale cloud pattern as shown in Fig. 2a. In this box, the reconstructed WVP pattern closely resembles that of reconstructed CWP but with a larger fluctuation amplitude. The scale of reconstructed rain rate fluctuation follows that of CWP but with much more concentrated peaks (Fig. 3i), implying a non-linear relationship between CWP and rain rate as will be discussed in Section 5.

Figs. 1-3 show that the db3 wavelet transform is capable of decomposing and reconstructing the multi-scale variability of CWP, WVP, and rain rate. A lower order wavelet such as db1 does not adequately remove large-scale WVP gradients, so it proves unsuitable for this analysis.

4. Dependence of MCC properties on cellular scale

Wavelet decomposition enables the isolation of mesoscale CWP and WVP fluctuations at each wavelength octave. Zhou and Bretherton (2019a&b) suggested that the growth and maintenance of MCC is tightly connected to mesoscale moisture anomalies, so one would expect a strong positive correlation between WVP and CWP when filtered to the dominant MCC scale (80 km in this box).

Figure 4 shows a scatterplot of wavelet-decomposed WVP vs. CWP fluctuations of the four wavelength octaves (20 km, 40 km, 80 km, and 160 km) in the 16 x 16 example box (256 grid-points) shown in Fig. 1. Indeed, in this box, chosen as a particularly nice example, the decomposed WVP fluctuation shows a strong linear relationship with its CWP counterpart at the diagnosed MCC scale of 80 km (level 3) with a correlation coefficient of 0.92 and a slope near 6. This correlation slope is very close to the median slope for all closed cells of 80 km scale (6.7) as will be shown in Fig. 5. The correlations at the other three wavelengths (20 km, 40 km, and 160 km) are more scattered. Although there are 256 grid-points, the octave-filtering reduces the effective degrees of freedom, which are controlled by the number of detail coefficients that contribute to each plot (192, 48, 12, and 3 for levels 1-4, respectively). Even so, the WVP-CWP relationship at 80 km is striking and drives most of the linear relation between WVP and CWP filtered to all four levels combined (compare the dashed line in Fig. 4 with the solid line).

To get a more robust statistical perspective, we classify the closed and open cell properties by dominant MCC scale (identified from CWP wavelet variance) within each 16 x 16 box in our three regional data samples. Fig. 5 presents this analysis using box-and-whisker plots separated by MCC scale. The numbers along the whiskers in Fig. 5a show the frequency of occurrence of closed and open cells of the different scales; 40 km and 80 km MCC scales occur most frequently. We already noted that 20 km wavelength cells can be difficult to detect using AMSR-E since they are not well resolved by the footprint of the CWP retrieval, so they may occur more frequently than this analysis suggests.

There is surprisingly little difference in the PDFs of box-mean CWP, WVP, and rain rate between boxes with MCC of scales 40, 80 and 160 km (Figs. 5a-5c). For each MCC scale, the differences between the PDFs of box-mean CWP and box-mean WVP for closed vs. open cells are modest but clear. Closed cells of each scale tend to have slightly higher mean CWP than open cells, but their area-mean rain rate tends to be lower than for open cells (as explained below). For 20 km MCC scale, the CWP and rain rate tend to be slightly lower compared to greater scales.

We filter the CWP and WVP data within each box to the MCC scale and perform statistics on those perturbations. The CWP standard deviation is similar for MCC scales of 40 km to 160 km (Fig. 5d), for which it corresponds to a typical CWP perturbation amplitude of 0.02-0.035 mm. The lowest CWP standard deviations for closed and open cells occur at 20 km, where they are usually comparable to the noise RMS of 0.017 mm, making the MCC difficult to distinguish from a quasi-

homogeneous cloudy layer with microwave data, even if it is evident on visible imagery. Overall, 20 km MCC scale usually occurs in cloud layers with low CWP and weak precipitation.

The CWP standard deviation is slightly higher in open than closed cells of all scales, implying that open cells are more inhomogeneous and are locally thicker. This generates patches of more intense precipitation that lead to the higher area-mean rain rate noted in Fig. 5c.

The WVP standard deviation has a much redder distribution across scales than the CWP standard deviation. It is significantly less than the detection threshold of 0.57 mm for MCC scales of 20 km and 40 km. Indeed, since the AMSR-E WVP has a 27 km footprint (Section 2.2), WVP perturbations at 20 km scale are meaningless, and at 40 km scale they are still not well-resolved. WVP standard deviation increases at larger MCC scales, but this is not primarily a consequence of MCC for which the CWP standard deviation maintains similar (Fig. 5d). In general, WVP variability is larger at longer wavelengths (e.g., 160 km), regardless of the MCC cell scale (not shown), suggesting that it is also responding to other large-scale dynamical processes in the free troposphere and boundary layer.

For each 16 x 16 box, we perform a linear regression of the WVP perturbations on the CWP perturbations at the MCC scale, obtaining a regression slope for that box. We choose CWP as the predictor for this regression because it's horizontal variability is more predominantly due to the MCC than for WVP. A box-whisker plot of the resulting slopes binned by MCC scale is shown in Fig. 5f. The regression slope dWVP'/dCWP' (WVP' and CWP' are the wavelet-filtered WVP and CWP fluctuations at a certain scale) is low (~4) at 20 km and 40 km. As discussed above, the WVP perturbations are unreliable at those scales, but the slope is nevertheless usually positive. At an MCC scale of 80 km, the slope increases to ~ 8, which is very close to that found in numerical simulations by Zhou and Bretherton (2019a). The slope slightly increases to ~ 10 at MCC scales of 160 km, but it is much more scattered, because the WVP perturbations are dominated by other processes and the CWP variability is not predominantly associated with individual mesoscale cells.

5. Non-linear relationship between CWP and rain rate

Comparison of maps of CWP (e.g. Fig. 3a) with rain rate (Fig. 3c) suggest a strong but nonlinear relationship, with rain restricted to regions of high CWP as physically expected. Note that CWP and our rain rate estimate are derived from different microwave bands, so this is not an artifact of the sensors and retrieval. Fig. 6 quantifies this relationship, showing the quartiles of CWP in bins of rain rate for AMSR-E ~10 km x10 km grid-points in closed and open MCC over the NE Pacific, SE

Pacific, and SE Atlantic for 2008. The rain rate (in mm day^{-1}) tends to increase cubically with CWP (in mm), with the composite fit shown in Fig. 6:

$$RR_{comp} \sim 300 \cdot CWP^3 \quad (1)$$

Surprisingly, this relationship fits both closed and open cells, especially for LWP above 0.25 mm. This suggests that the rain rate for the thicker clouds in open and closed cells is dominated by CWP with little modulation from aerosols. Open cells create local regions with greater CWP and therefore higher peak rain rates. Note that if the underestimation of the AMSR-E CWP above 180 g m^{-2} is considered (Section 2.2), the dependence of rain rate on CWP would be less steep.

6. Environmental control on MCC scale

To investigate potential environmental controls on MCC scale, we bin some candidate factors (PBL depth, SST, EIS, and 10 m wind speed) by MCC scale for closed and open cells, as in Fig. 5. Fig. 7a shows that bin-median PBL depth increases appreciably (from ~ 1 km to ~1.5 km) from 20 km to 40 km MCC, stays around 1.5 km for 80 km MCCs, and slightly lowers for 160 km scales. Our result corroborates Wood and Hartmann (2006) in that small MCC tends to be associated with shallow PBLs, but we do not find a positive correlation between PBL depth and MCC scale beyond 40 km. This may reflect differences between their MODIS-based approach to quantifying MCC scale and our microwave-based approach and merits further study. The slight decrease in PBL depth for 160 km scales may be an artifact; what is classified as a 160 km scale MCC is often a boundary between patches of smaller cells in cloudier and clearer air masses rather than a single cell (see Section 3.2). The impacts of SST, EIS, and 10 m wind on the MCC scale are marginal (Figs. 7b-7d). Furthermore, we found no significant geographical control on cloud scale in the three regions (Figs. S1 and S2).

Environmental controlling factors appear to be more important in distinguishing closed and open cells than in setting their scale. At all MCC scales, open cells are associated with deeper PBL, warmer SST, lower EIS and higher 10 m wind speed (Figs. 7a-7d), suggesting that open cells tend to occur over warmer ocean farther away from the coast (as in Agee et al., 1973) where inversion strength is weaker (as in McCoy et al., 2017), the boundary layer is deeper (as in Wood and Hartmann, 2006), and the trade winds are stronger. Open cells tend to also be associated with higher 10-m wind speed compared to closed cells at all MCC scales (Fig. 7d), although the majority of the data between closed and open cells heavily overlap. This is consistent with Eastman et al. (2021), who found that open cells tend to occur in a higher wind-speed environment. Since warm SST and

strong winds are primary drivers of surface fluxes, it is likely that closed to open cells transition is inclined to be facilitated in strong surface flux conditions. Unsurprisingly, open cells favor locations further downwind into the climatological transition from stratocumulus to cumulus (Fig. S2), as also found by Wood and Hartmann (2006), Muhlbauer et al. (2014), and McCoy et al. (2017).

7. Mesoscale cell composite

So far we have shown that within cells, CWP is correlated to rain rate and its background mesoscale-filtered WVP. Using the derived slope S of WVP fluctuations regressed onto CWP fluctuations in the 16 x 16 pixel boxes, a WVP composite (WVP_{comp}) is obtained as:

$$WVP_{comp} = S \cdot CWP' + \overline{WVP} \quad (2)$$

Here, CWP' is a representative CWP fluctuation across a cell, and $\overline{WVP}$ is the domain-averaged WVP. We can also compute a rain rate composite using the cubic polynomial relation (1) between rain rate and CWP. This allows a 'composite' WVP and rain rate for MCC of a particular scale to be estimated solely from typical CWP variations at that scale. We use a scale of 80 km as an example since it typically has the largest CWP variance, and it is well above the AMSR-E footprint resolution of CWP and WVP, and hence provides trustworthy CWP and WVP variability and co-variability.

The WVP and rain rate composites are not just statistical summaries; they can also be good representations of WVP and rain rate for individual cases. Fig. 8 shows a closed cell case (the same as the example box in Fig. 1). The 20-160 km reconstructed CWP, WVP, and rain rate in Figs. 8a-c are computed as the sum of their box means and their wavelet-filtered fluctuations at the four finest octave scales. These realistically represent the cloud, humidity, and rain rate variability within the example box. The reconstructed CWP , WVP, and rain rate at 80 km in Figs. 8d-f are computed as the sum of the 80 km wavelet-filtered fluctuations and their box means. Comparing Fig. 8a with Fig. 8d shows that for this particularly clean closed-cell case, the 80 km reconstructed CWP, WVP, and rain rate are good representations of their overall mesoscale variations within the 16 x 16 example box.

The WVP composite in Fig. 8h is computed following Eq. (2), using the median correlation slope derived for the 80-km closed cells (6.7, as shown in Fig. 5f), and using the 80 km CWP perturbation in Fig. 8d as a representative 'composite' CWP for this typical closed cell. The composite WVP compares qualitatively well with the actual 80-km reconstructed WVP for the closed cell shown in

Fig. 8e. The rain rate composite in Fig. 8i is computed from the 80 km reconstructed CWP using Eq. (1); again it agrees well with the actual 80 km reconstructed rain rate for this case.

The correlations between reconstructed and composite WVPs and rain rates are equally strong for open cells. An example of a box with 80-km scale open cell convection observed over the SE Pacific region on 19 October 2008 is shown in Fig. 9, using the same format as in Fig. 8. The polygonal patterns of cumulus characteristic open-cell organization is obvious on the MODIS image but is not clear in the lower-resolution microwave data, even in the full 20-160 km reconstructed fields. The magnitudes of the CWP variations are similar to the closed-cell example. Both the reconstructed 80 km variability and the 'composite' variability in WVP and rain rate also look qualitatively similar to the closed-cell example. The open-cell composite uses a slightly larger regression slope S = 8 to relate 80 km WVP perturbations to CWP perturbations than for closed cells, based on Fig. 5f.

Figs. 8 and 9 demonstrate that the 80-km scale WVP and rain rate perturbations for a typical 80 km open or closed cell can be estimated from its 80 km CWP variations. Here we build a statistical composite based on all 80-km scale closed and open cells over three regions observed in 2008. We use 80 km cells because they are both common and well-resolved by all the AMSR-E retrievals, including WVP. We build idealized sinusoidal CWP and WVP sections across a typical 80-km scale closed and open cell. For each cell type, the wave mean is chosen as the median box mean and the wave amplitude (denoted ΔCWP or ΔWVP) is $2^{1/2}$ times the median standard deviation (since the standard deviation of a uniformly sampled sinusoid of amplitude a is $2^{-1/2}a$). The maximum and minimum of the sinusoidal CWP wave represent the cloud centers and cloud edges respectively.

The bottom part of Fig. 10 shows the resulting closed and open cell composites,. The median composites, shown as the solid red lines, are computed from Fig. 5 as follows. Fig. 5a implies the bin-mean CWP is 0.075 mm for 80 km closed cells and 0.065 mm for 80 km open cells. Fig. 5d implies that the median standard deviation of CWP is 0.026 mm and 0.033 mm for 80 km closed and open cells, so the CWP sinusoid amplitude is 1.4 times as large -- 0.037 mm for closed cells and 0.047 mm for open cells. Thus the CWP ranges from 0.038-0.112 mm across the composite closed cell and 0.018-0.112 mm across the composite open cell. Note that because we are only considering variability at a single scale (80 km), we do not expect a minimum composite CWP = 0 (no cloud) even in the driest part of open cells, which are usually nearly cloud-free.

The red shading in Fig. 10 indicates the range of CWP composites obtained by using the envelope of interquartile ranges of CWP standard deviation from the boxes in Fig. 5d (0.02-0.035 mm for closed cells and 0.023-0.045 mm for open cells) in place of its median, showing expected natural variability

of MCC around this composite. Another source of variability is the box-mean CWP, which has an interquartile range of 0.05~0.1 mm for both open and closed cells that affects both the composite mean and perturbation rain rate. We represent this source of variability in the CWP composites by adding the 25^{th} to 50^{th} quartile range of the box mean above the top of the shading, and the 50^{th} to 75^{th} quartile range below the bottom of the shading (dashed lines in Fig. 10, shown only where they are above zero, indicating some cloud is present). The dashed lines mark an envelope including interquartile ranges of both amplitudes and box means.

Multiplying the median CWP standard deviations by the median correlation slopes in Fig. 5f (6.7 for 80 km closed cells and 8 for open cells), we get a median WVP standard deviation of 0.17-0.24 mm and hence sinusoid amplitudes of 0.25-0.4 mm for 80 km closed and open cells respectively. Adding the median of the box-mean WVP for each case gives the WVP composite (black curves). The nature variability of the WVP composite is marked by the gray shading, computed by multiplying the interquartile range of CWP standard deviations by the median correlation slopes in Fig. 5f. The box-mean WVP varies so much across our sampling regions and seasons that we do not show this on Fig. 10.

The rain rate composites are computed from the CWP composite following the cubic relation given in Eq. (1). The median CWP sinusoid (red curve) generates the median rain-rate curve (blue curve), the red-shaded range of CWP sinusoids generates the blue-shaded range of rain rate, and the red dashed curve incorporating interquartile variability in both the CWP box-mean and cell-scale perturbation amplitude generates the blue dashed curve. The rain rate varies over a larger relative range than CWP due to its cubic dependence of CWP.

The CWP and rain rate are comparable in the thick part of the median open and closed cells, although there is a lot of variability around the median composites (Fig. 10). The more intense open cells have walls of thicker CWP with more intense precipitation than typically seen in closed cells (as seen from the largest shaded CWP and rain rates in the bottom panel of Fig. 10). The box-mean contribution to CWP is also an important source of variability, contributing especially to some cells raining a lot more than others (compare bottom and top blue dashed lines). In the thinnest part of the open cell CWP composites, the shaded region extends down nearly to CWP = 0 and when also considering the box mean variability, much of the drier portions of many open cells have CWP = 0 (cloud-free), consistent with visible satellite imagery.

The upper part of Fig. 10 shows schematics for 80 km closed and open cell MCC. For each cell type, the CWP and rain rate at the cloud centers and edges in the schematics are computed from the

maximum and minimum of the sinusoidal composites. The relative humidity perturbations (ΔRH) are computed as $\Delta WVP/WVP_{sat}$, where ΔWVP is taken from the sinusoidal composite for that cell type and WVP_{sat} is the saturation WVP in the PBL (estimated as 15 mm or 15 kg m^{-2} of water, based on a representative PBL saturation mixing ratio of 10 g/kg and a PBL column dry air mass of 1500 kg m^{-2}, corresponding to a 150 hPa pressure thickness). For both closed and open cells, ΔWVP is 0.25~0.35 mm so ΔRH ~ 2%. On average, the median closed and open cell composites are nearly indistinguishable using only the AMSR-E data, even though open and closed cells are readily distinguishable in finer resolution MODIS visible imagery.

Discussion and conclusion

We have applied a two-dimensional discrete wavelet transform to AMSR-E passive microwave data to study mesoscale cellular convection in subtropical marine low clouds and its relationship with environmental factors. The key AMSR-E fields used are cloud water path (CWP), water vapor path (WVP), and rain rate (RR). The wavelet analysis partitions the variability and co-variability of these three fields within 160x160 km subregions ('boxes') of each data swath into four octave scales, corresponding to representative wavelengths of 20, 40, 80, and 160 km. We use this partitioning to identify a dominant local scale of mesoscale CWP variability in each box, when present. The most common cell scales are 40-80 km. For cells of these scales, we find that cell-scale CWP perturbations are well correlated with WVP and rain rate perturbations, allowing us to create a composite cell structure. A machine learning scheme based on MODIS CWP is used to classify cells into open, closed or other, allowing us to compare the statistics and composite structure of open and closed cells.

The microwave composites are surprisingly similar for open and closed cells despite their clearly different appearance on the much finer resolution MODIS visible imagery. Closed cells have a slightly higher box-mean CWP and slightly less cell-scale CWP variability. A cubic relationship between rain rate and CWP is descriptive for both cell types. This suggests that variations in aerosol concentrations and cloud droplet concentrations may not be a primary control of cell type, since that would create a different susceptibility of precipitation to CWP in open vs. closed cells. This is an interesting counterpoint to well-documented examples of pockets of open cells (e.g., Wang and Feingold, 2009; Savic-Jovcic and Stevens, 2008) in which a transition from closed to open cells is associated with dramatic precipitation-induced aerosol loss that causes much lower droplet concentrations in the pocket of open cells than in the surrounding overcast stratocumulus.

Our analysis suggests that MCC scales of 40 km and larger are uncorrelated with box-mean CWP, WVP, rain rate, or PBL depth, in contrast to a MODIS-based analysis by Wood and Hartmann (2006) showing a 40:1 ratio of cell scale to PBL depth. MCC of smaller 20 km scale usually occurs in a shallower boundary layer (~1 km) with clouds that are thinner, more homogeneous, and less drizzly. All cell scales have similar geographic distribution.

Our results indicate that SST, EIS, and 10-m wind speed do not play a major role in determining the scale of the MCC, which implies that the increase of cell scale might stem more from its historical evolution than from the environmental conditions at the time of measurement. As in past studies (e.g., Agee et al., 1973; Wood and Hartmann 2006; Muhlbauer et al., 2014, McCoy et al., 2017, Eastman et al., 2021), open cells favor somewhat deeper PBLs over warmer SST.

This study has several limitations. One of them is the broad 27 x 16 km footprint of the AMSR-E WVP that prevents us from resolving the moisture variability at small MCC wavelength (20 km and 40 km). Future spaceborne differential absorption radar has the potential to provide column WVP at much higher spatial resolution than is currently possible (Millán et al., 2020). The WVP also cannot disentangle moisture variability in the boundary layer from that in the free troposphere, although multi-sensor studies combining MODIS and AMSR-E could be used in future to remove the free-tropospheric contribution to the column water vapor (Millán et al., 2019). The 14 x 8 km CWP footprint is also much coarser than MODIS (~1 km) and cannot resolve narrow cloud bands typical of open cells (e.g., Fig. 9). In addition, the WVP and (to a lesser extent) CWP retrievals are not sensitive enough to detect weak cellular variability and thin and/or broken cloud. Furthermore, the current MCC classification is conservative in labeling some low-coverage closed cells as open cells. This might partially explain the resemblance of the statistics between closed and open cells in this study. It might be interesting to explore use of this wavelet methodology on MODIS-based visible wavelength retrievals of CWP matched to the microwave data. In particular, this might shed light on the apparent discrepancy with Wood and Hartmann's conclusions about cell scale dependence on PBL depth. It might also be interesting to use similar wavelet-based techniques on MCC associated with extratropical cyclones in the storm tracks.

REFERENCES:

Abel, S. J., Boutle, I. A., Waite, K., Fox, S., Brown, P. R., Cotton, R., ... & Bower, K. N. (2017). The role of precipitation in controlling the transition from stratocumulus to cumulus clouds in a Northern Hemisphere cold-air outbreak. *J. Atmos. Sci.*, *74*, 2293-2314.

Abel, S. J., Barrett, P. A., Zuidema, P., Zhang, J., Christensen, M., Peers, F., ... & Flynn, M. (2020). Open cells exhibit weaker entrainment of free-tropospheric biomass burning aerosol into the south-east Atlantic boundary layer. *Atmospheric Chem. Phys. (Online)*, *20*.

Agee, E. M., Chen, T. S., & Dowell, K. E. (1973). A review of mesoscale cellular convection. *Bull. Amer. Meteor.*, *54*, 1004-1012.

Agee, E. M. (1984). Observations from space and thermal convection: A historical perspective. *Bull. Amer. Meteor.*, *65*, 938-949.

Atkinson, B. W., & Wu Zhang, J. (1996). Mesoscale shallow convection in the atmosphere. *Rev. Geophys.*, *34*, 403-431.

Berner, A. H., Bretherton, C. S., Wood, R., & Muhlbauer, A. (2013). Marine boundary layer cloud regimes and POC formation in a CRM coupled to a bulk aerosol scheme. *Atmos. Chem. Phys.*, *13*.

Boutle, I. A., & Abel, S. J. (2012). Microphysical controls on the stratocumulus topped boundary-layer structure during VOCALS-REx. *Atmos. Chem. Phys.*, *12*, 2849–2863. https://doi.org/10.5194/acp-12-2849-2012.

Bretherton, C. S., & Wyant, M. C. (1997). Moisture transport, lower-tropospheric stability, and decoupling of cloud-topped boundary layers. *J. Atmos. Sci.*, *54*, 148-167.

Daubechies, I. (1988). Orthonormal bases of compactly supported wavelets. *Commun. Pure Appl. Math.*, *41*, 909-996.

Daubechies, I., & Bates, B. J. (1993). Ten lectures on wavelets.

Dee, D. P., Uppala, S. M., Simmons, A. J., Berrisford, P., Poli, P., Kobayashi, S., ... & Bechtold, P. (2011). The ERA-Interim reanalysis: Configuration and performance of the data assimilation system. *Q. J. R. Meteorol. Soc.*, **137**, 553-597.

569 Eastman, R., Lebsock, M., & Wood, R. (2019). Warm Rain Rates from AMSR-E 89-GHz Brightness
570 Temperatures Trained Using CloudSat Rain-Rate Observations. *J. Atmos. Ocean. Technol.*, ***36***,
571 1033-1051.
572 Eastman, R., & Wood, R. (2016). Factors controlling low-cloud evolution over the eastern subtropical
573 oceans: A Lagrangian perspective using the A-Train satellites. *J. Atmos. Sci.*, ***73***, 331-351.
574 Eastman, R., Wood, R., & Ting O, K. (2017). The subtropical stratocumulus-topped planetary boundary
575 layer: A climatology and the Lagrangian evolution. *J. Atmos. Sci.*, *74*, 2633-2656.
576 Eastman, R., et al., McCoy, I. L., and Wood, R. J. (2021). Environmental and internal controls on
577 Lagrangian transitions from closed cell mesoscale cellular convection over subtropical oceans. J.
578 Atmos. Sci.
579 Field, P. R., Cotton, R. J., McBeath, K., Lock, A. P., Webster, S., & Allan, R. P. (2014). Improving a
580 convection‐permitting model simulation of a cold air outbreak. *Q. J. R. Meteorol. Soc.*, *140*, 124-
581 138.
582 Fletcher, J., Mason, S., & Jakob, C. (2016). The climatology, meteorology, and boundary layer structure of
583 marine cold air outbreaks in both hemispheres. *J. Climate*, *29*, 1999-2014.
584 Goren, T., & Rosenfeld, D. (2012). Satellite observations of ship emission induced transitions from broken
585 to closed cell marine stratocumulus over large areas. *J. Geophys. Res. Atmos.*, *117*.
586 King, M. D., Kaufman, Y. J., Menzel, W. P., & Tanre, D. (1992). Remote sensing of cloud, aerosol, and
587 water vapor properties from the Moderate Resolution Imaging Spectrometer (MODIS). *IEEE*
588 *Trans. Geosci. Remote Sens.*, ***30***, 2-27.
589 King, M. D., Menzel, W. P., Kaufman, Y. J., Tanré, D., Gao, B. C., Platnick, S., ... & Hubanks, P. A.
590 (2003). Cloud and aerosol properties, precipitable water, and profiles of temperature and water
591 vapor from MODIS. *IEEE Trans. Geosci. Remote Sens.*, *41*, 442-458.
592 Kumar, P., & Foufoula‐Georgiou, E. (1997). Wavelet analysis for geophysical applications. *Rev.*
593 *Geophys.*, ***35***, 385-412.
594 Kummerow, C., Ferraro, R., & Randel, D. (2015). AMSR-E/Aqua L2B Global Swath Surface Precipitation
595 GSFC Profiling Algorithm, version 3.

596 Mallat, S. G. (1989a). A theory for multiresolution signal decomposition: the wavelet representation. *IEEE*
597 *Trans. Pattern Anal Mach Intell., 11*, 674-693.
598 Mallat, S. G. (1989b). Multifrequency channel decompositions of images and wavelet models. *IEEE Trans.*
599 *Acoust.,, 37*, 2091-2110.
600 McCoy, I. L., Wood, R., & Fletcher, J. K. (2017). Identifying meteorological controls on open and closed
601 mesoscale cellular convection associated with marine cold air outbreaks. *J. Geophys. Res. Atmos.*,
602 **122**, 11-678.
603 Meyer, Y. (1992). *Wavelets and Operators: Volume 1* (Vol. 37). Cambridge University Press.
604 Millán, L. F., Lebsock, M. D., and Teixeira, J.: Variability of bulk water vapor content in the marine cloudy
605 boundary layers from microwave and near-infrared imagery, *Atmos. Chem. Phys*., 19, 8491–8502,
606 https://doi.org/10.5194/acp-19-8491-2019, 2019
607 Millán, L., Roy, R., and Lebsock, M.: Assessment of global total column water vapor sounding using a
608 spaceborne differential absorption radar, *Atmos. Meas. Tech.*, 13, 5193–5205,
609 https://doi.org/10.5194/amt-13-5193-2020, 2020.
610 Muhlbauer, A., McCoy, I. L., & Wood, R. (2014). Climatology of stratocumulus cloud morphologies:
611 microphysical properties and radiative effects. *Atmos. Chem. Phys*., *14*.
612 Sandu, I., & Stevens, B. (2011). On the factors modulating the stratocumulus to cumulus transitions. *J.*
613 *Atmos. Sci., 68*, 1865-1881.
614 Savic-Jovcic, V., & Stevens, B. (2008). The structure and mesoscale organization of precipitating
615 stratocumulus. *J. Atmos. Sci.*, *65*, 1587-1605.
616 Seethala, C., & Horváth, Á. (2010). Global assessment of AMSR‐E and MODIS cloud liquid water path
617 retrievals in warm oceanic clouds. *J. Geophys. Res. Atmos.*, *115*.
618 Sharon, T. M., Albrecht, B. A., Jonsson, H. H., Minnis, P., Khaiyer, M. M., van Reken, T. M., ... & Flagan,
619 R. (2006). Aerosol and cloud microphysical characteristics of rifts and gradients in maritime
620 stratocumulus clouds. *J. Atmos. Sci.*, *63*, 983-997.
621 Siebesma, A. P., Bretherton, C. S., Brown, A., Chlond, A., Cuxart, J., Duynkerke, P. G., ... & Sanchez, E.
622 (2003). A large eddy simulation intercomparison study of shallow cumulus convection. *J. Atmos.*
623 *Sci., **60***, 1201-1219.

Stevens, B., Vali, G., Comstock, K., Wood, R., Van Zanten, M. C., Austin, P. H., ... & Lenschow, D. H. (2005). Pockets of open cells and drizzle in marine stratocumulus. *Bull. Amer. Meteor., 86*, 51-58.

Turner, D. D., Clough, S. A., Liljegren, J. C., Clothiaux, E. E., Cady-Pereira, K. E., & Gaustad, K. L. (2007). Retrieving Liquid Wat0er Path and Precipitable Water Vapor From the Atmospheric Radiation Measurement (ARM) Microwave Radiometers. *IEEE Trans. Geosci. Remote Sens., 45*, 3680-3690.

Wang, H., & Feingold, G. (2009). Modeling mesoscale cellular structures and drizzle in marine stratocumulus. Part I: Impact of drizzle on the formation and evolution of open cells. *J. Atmos. Sci., 66*, 3237-3256.

Wentz, F. J. and T. Meissner. 2004. *AMSR-E/Aqua L2B Global Swath Ocean Products derived from Wentz Algorithm, Version 2*. [Columnar cloud liquid water; columnar water vapor]. Boulder, Colorado USA. NASA National Snow and Ice Data Center Distributed Active Archive Center. doi: https://doi.org/10.5067/AMSR-E/AE_OCEAN.002.

Wood, R., & Bretherton, C. S. (2004). Boundary layer depth, entrainment, and decoupling in the cloud-capped subtropical and tropical marine boundary layer. *J. Climate, 17*, 3576-3588.

Wood, R., & Bretherton, C. S. (2006). On the relationship between stratiform low cloud cover and lower-tropospheric stability. *J. Climate*, *19*, 6425-6432.

Wood, R., and Hartmann, D. L., 2006. Spatial variability of liquid water path in marine low cloud: The importance of mesoscale cellular convection. *J. Climate*, **19**, 1748-1764.

Yamaguchi, T., & Feingold, G. (2015). On the relationship between open cellular convective cloud patterns and the spatial distribution of precipitation. *Atmos. Chem. Phys*, 15, 1237-1251.

Zhou, X., & Bretherton, C. S. (2019). Simulation of mesoscale cellular convection in marine stratocumulus: 2. Nondrizzling conditions. *J. adv. model., 11*, 3-18.

Zhou, X., & Bretherton, C. S. (2019b). The correlation of mesoscale humidity anomalies with mesoscale organization of marine stratocumulus from observations over the ARM Eastern North Atlantic Site. *J. Geophys. Res. Atmos., 124*, 14059-14071.

Figure 1

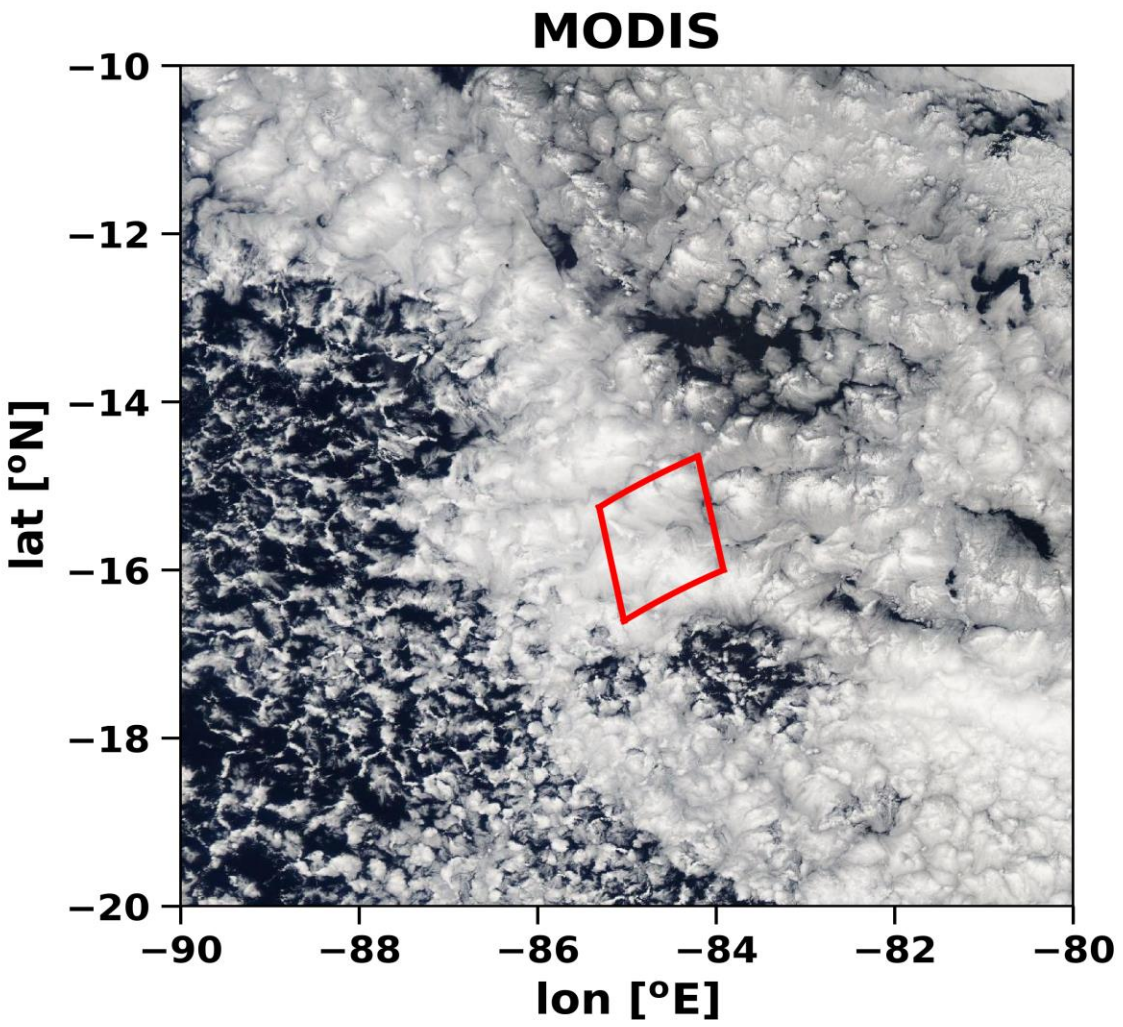

Fig. 1. MODIS 10º x 10º scene (~1110 km x 1110 km) at 1-km resolution at nadir over the SE Pacific on August 11, 2008, taken from NASA Worldview. An example closed-cell region of ~160 km x 160 km (discussed later) is denoted by a red box.

Figure 2

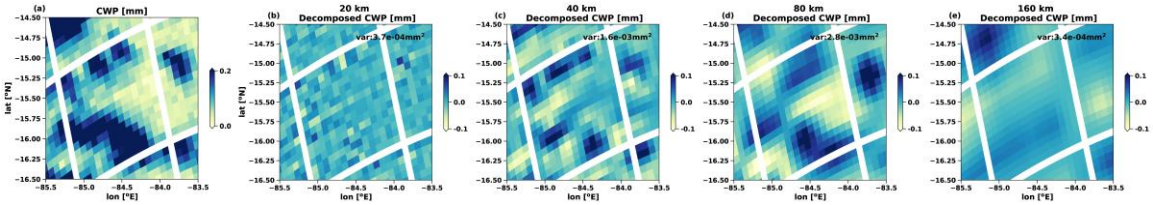

Fig. 2. (a) AMSR-E measured CWP in the example region shown in the red box of Figure 1. The white strips mark the border of the box and neighboring 16 x 16 pixel regions. (b-e) CWP fluctuations decomposed into wavelength octaves of (b) 20 km, (c) 40 km, (d) 80 km, and (e) 160 km. CWP variances of the four wavelength octaves are indicated on the upper right of each panel.

Figure 3

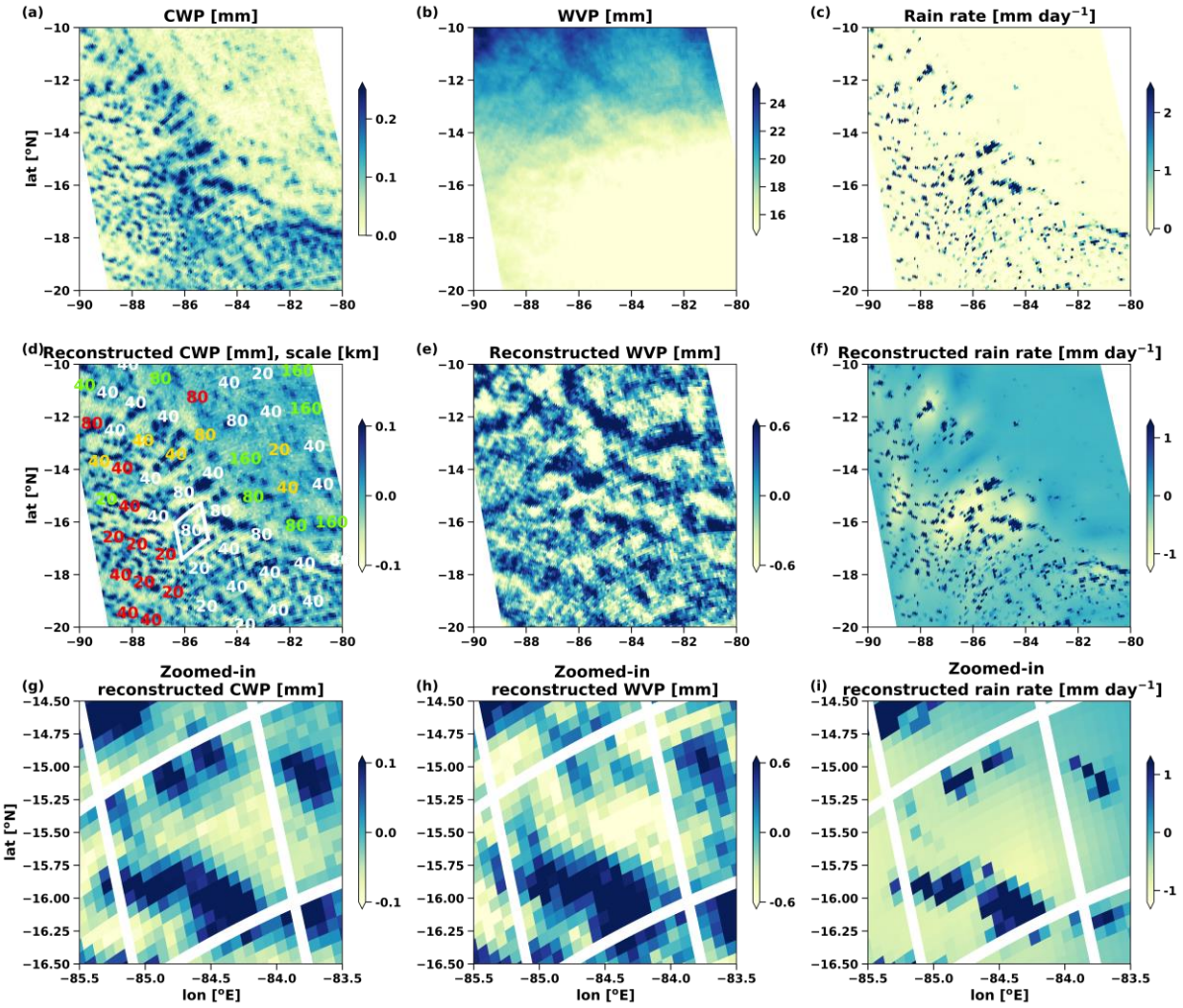

Fig. 3. (a) AMSR-E retrieved (a) CWP, (b) WVP, and (c) rain rate over the same scene as in Figure 1. The white gaps at the bottom left corners fall outside of the swath; those at the upper right corners are the result of data truncation. High-pass (d) CWP, (e) WVP, and (f) rain rate reconstructed from the detail coefficients of wavelength octaves 20 km to 160 km. The computed cloud scales in each 16 x 16 grid (~160 km x 160 km) box are indicated in (d). White, red, yellow, and green indicate closed, open, disorganized, and mixed pattern MCC respectively. In (d), the example closed-cell box from Fig. 1 is indicated in white. (g-i) Same as (d-f) but zoomed into the example closed-cell box. The white strips mark the border of the box and its neighbors.

679 Figure 4

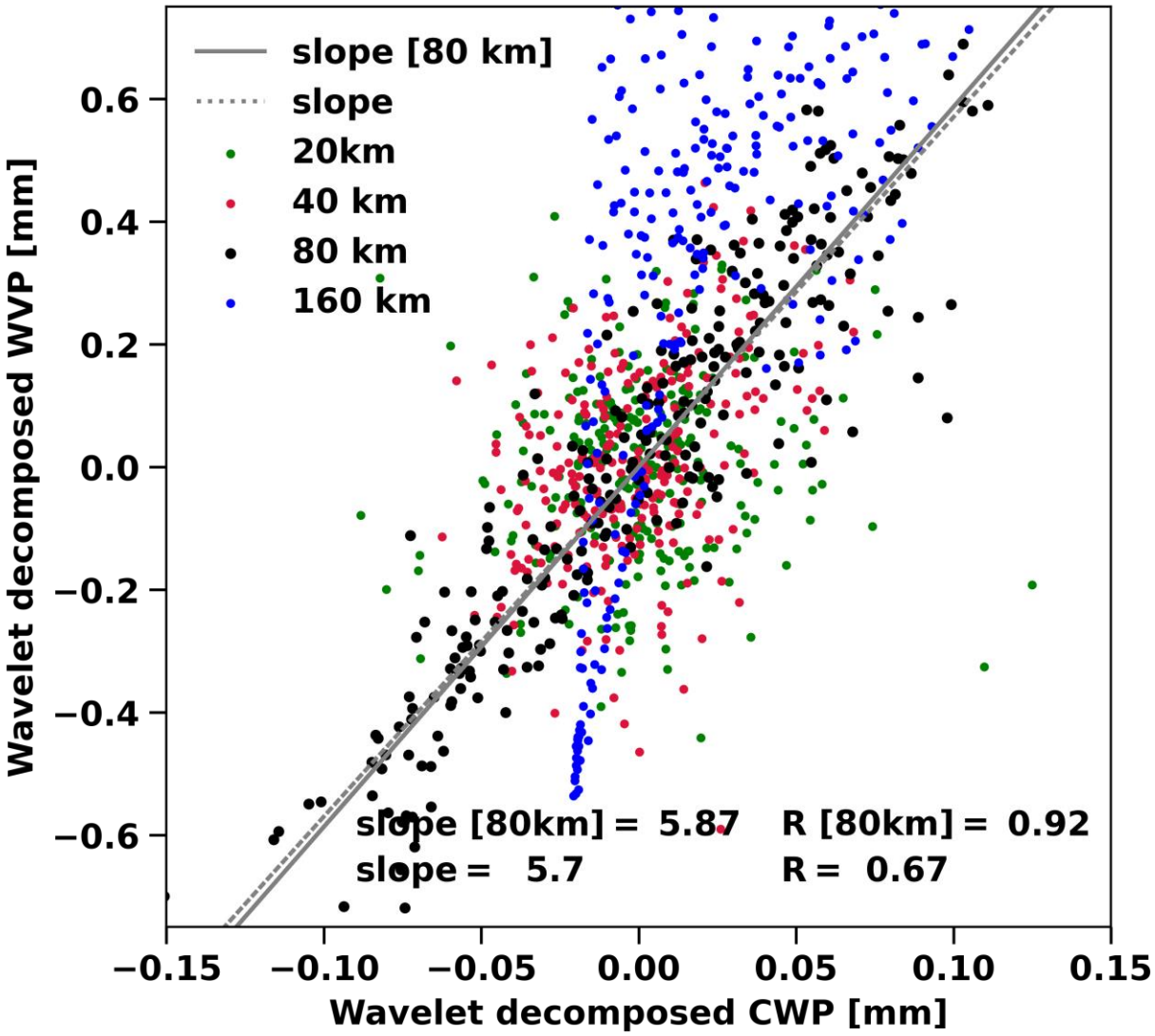

680

681 Fig. 4. Scatterplots of wavelet-decomposed CWP and WVP fluctuations for octaves of 20 km (green), 40 km (red), 80 km (black), and 160
682 km (blue). Least square fits through the origin (0,0) between fluctuations at wavelength 80 km and between fluctuations at all wavelengths
683 are shown as gray solid and dashed lines, respectively. Their slopes and correlation coefficients are shown near the bottom of the plot.

684

685

686

687

688

689

690

691

Figure 5

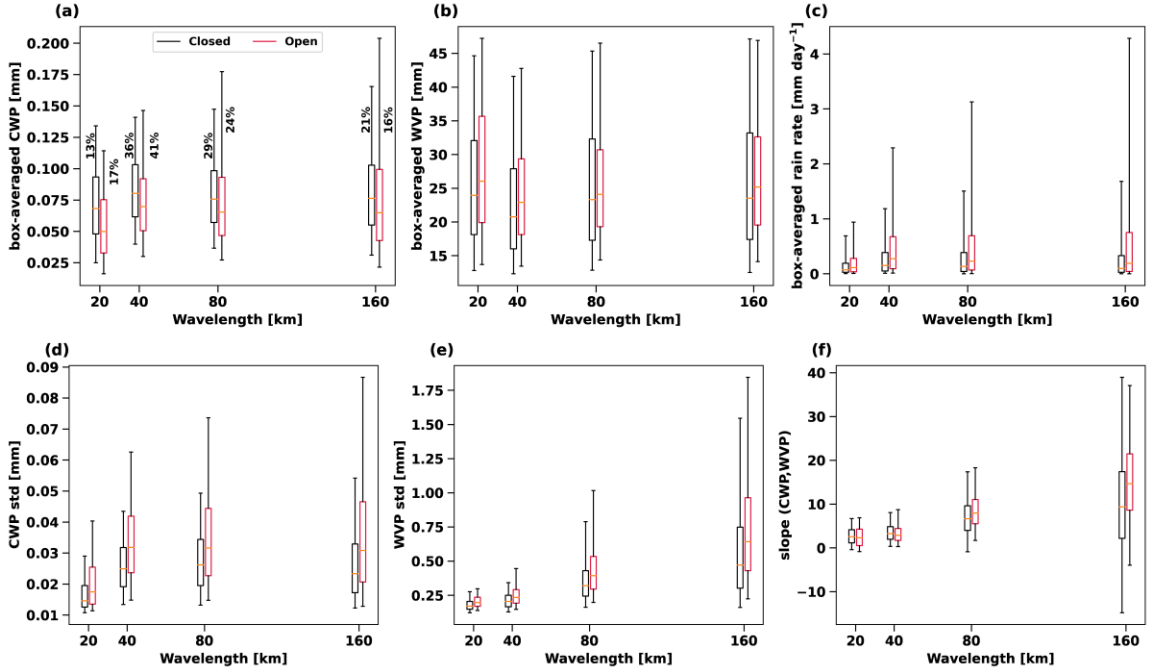

Fig. 5. The interquartile range (IQR; as indicated by the box plot) of (a) CWP, (b) WVP, (c) rain rate, (d) CWP standard deviation, (e) WVP standard deviation, and (f) slope of the least squares linear fits of WVP fluctuations onto CWP fluctuations for closed and open MCC with different scales, across all 2008 data in the three study regions. The CWP standard deviation, WVP standard deviation, and the slope are computed from the wavelet-decomposed WVP and CWP fluctuations in the octave of the wavelength. The orange bar inside each box indicates a bin-median value and the whiskers indicate a range of 5th to 95th quartile. The frequency of occurrence of each IQR box is shown in (a).

715 Figure 6

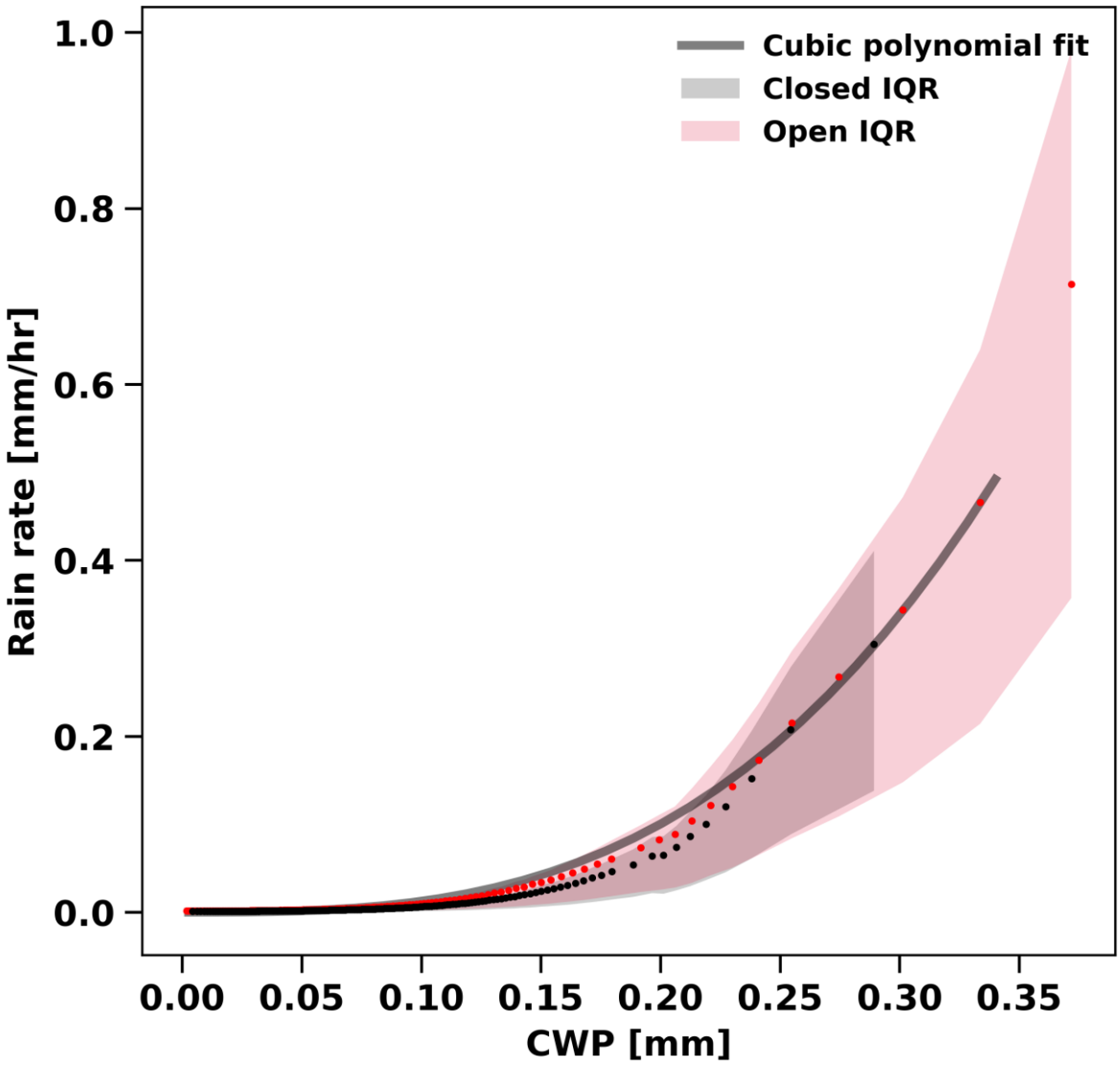

716

717 Fig. 6. Quartiles of CWP versus rain rate for closed and open MCC clouds over NE Pacific, SE Pacific, and SE Atlantic for 2008. Dots
718 indicate mean rain rate within CWP quartile bins (0.5%). Shading indicates the interquartile range. The cubic polynomial fit through origin
719 (0,0) for the full dataset including both closed and open cells is indicated by the solid grey line.

720

721

722

723

724

725

726

727

Figure 7

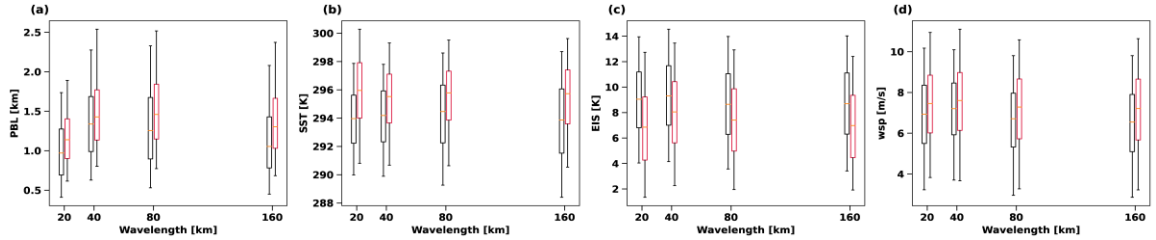

Fig. 7. Same as Fig. 5 but for (a) PBL height, (b) SST, (c) EIS, and (d) 10-m wind speed.

Figure 8

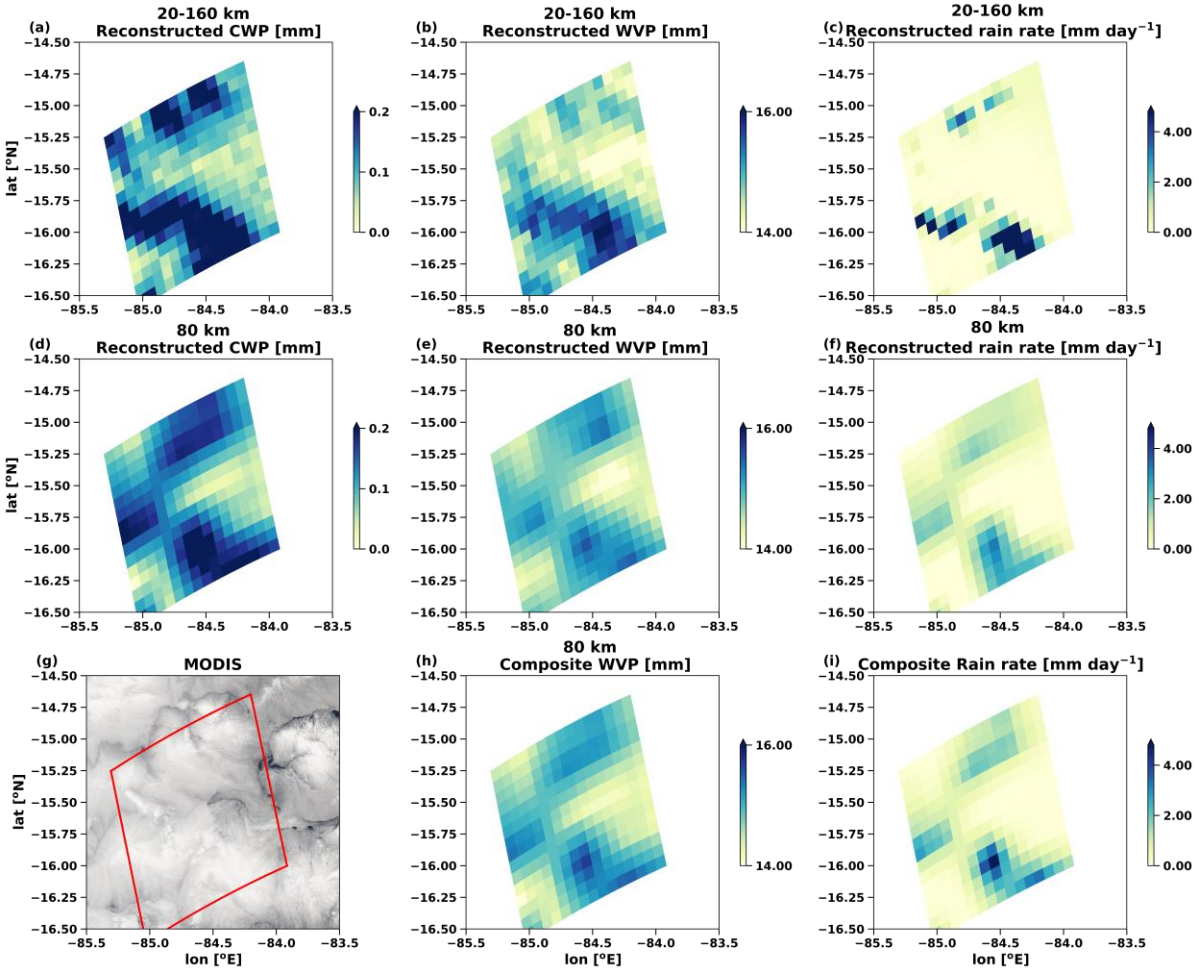

Fig. 8. 20-160 km wavelet-reconstructed (a) CWP, (b) WVP, and (c) rain rate. 80 km wavelet-reconstructed (d) CWP, (e) WVP, and (f) rain rate for the closed MCC of scale 80 km in the example box in Fig. 1. The corresponding MODIS scene is shown in (g). Composite (h) WVP and (i) rain rate computed from the 80 km CWP using Eqs. 2, and 1.

Figure 9

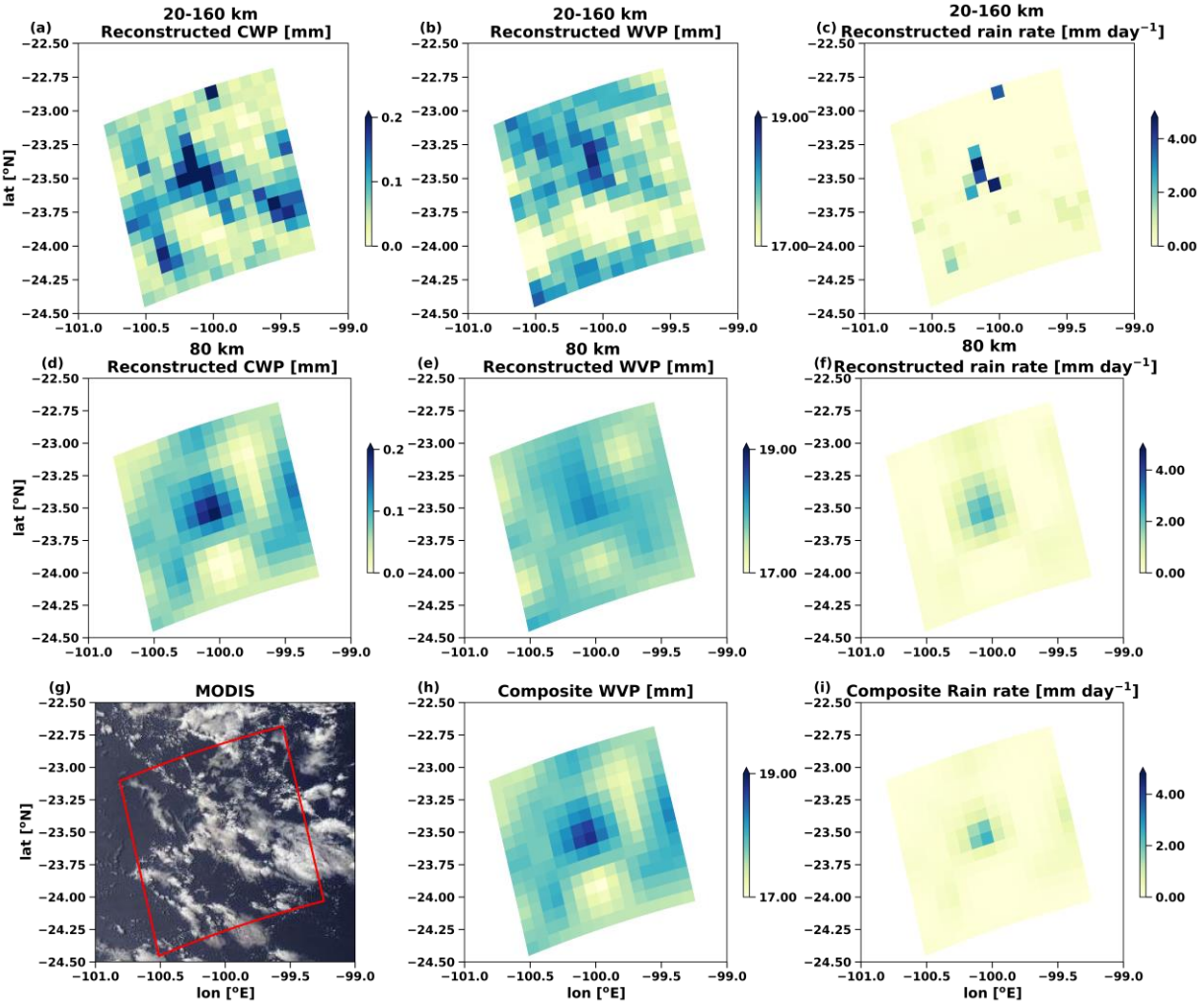

Fig. 9. Same as Fig. 8 but for an open cell case on 19 October, 2008 over SE Pacific.

754 Figure 10

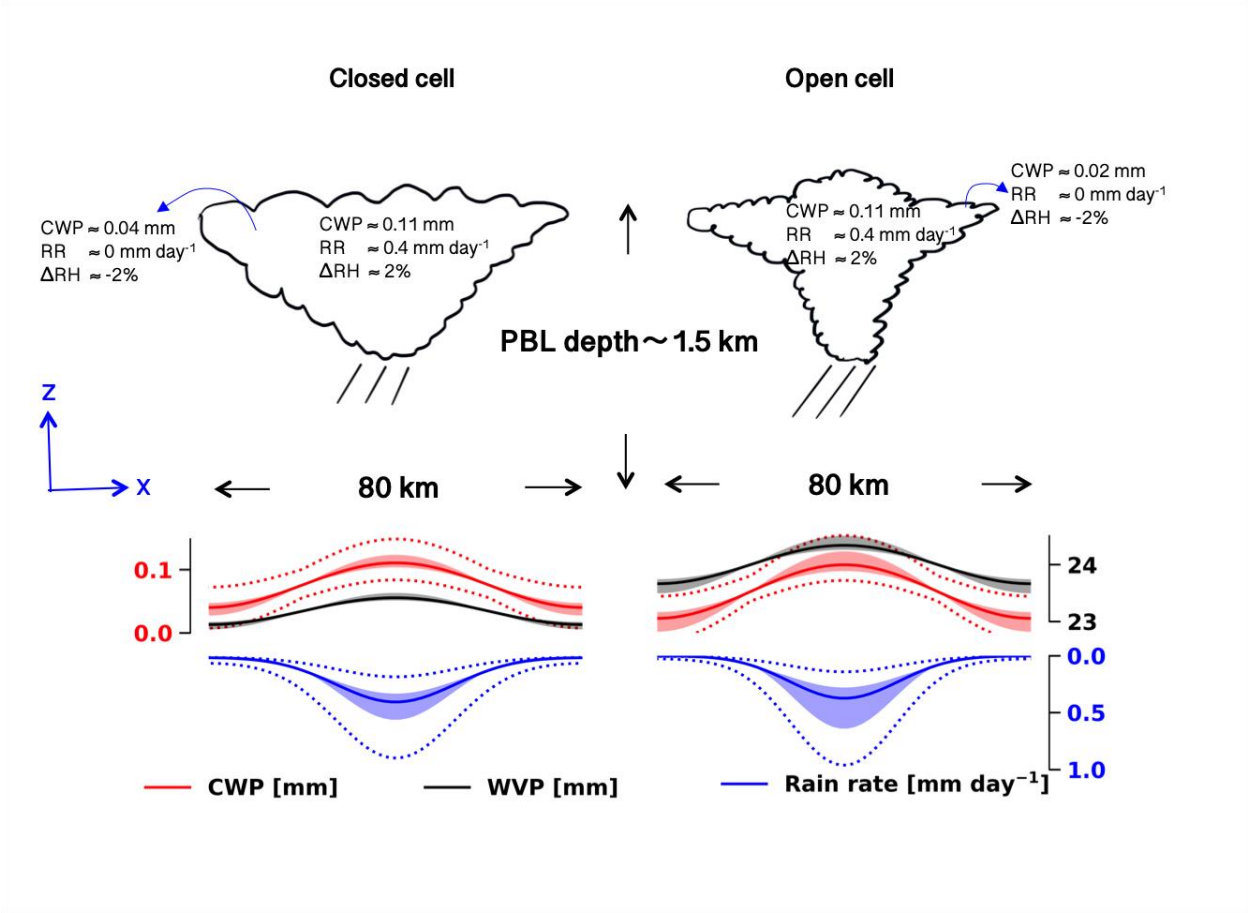

755

756 Fig. 10. The median values (solid line) of AMSR-E measured box-mean CWP, composite WVP computed from eq. 2 at 80 km, and
757 composite rain rate computed from eq. 1 for closed and open cells. The shading indicates the envelope of interquartile ranges of
758 amplitudes. The dashed lines mark a bigger envelope including interquartile ranges of both amplitudes and box means. The schematic of
759 closed and open cells together with the median values of box-mean CWP and rain rate (RR) at the centers and edges of the cells are also
760 shown. The relative humidity anomalies (ΔRH) are computed by assuming the saturation WVP in the PBL is 15 mm.

761

762

763

764

765

766

767

768

769

770

771

Figure S1

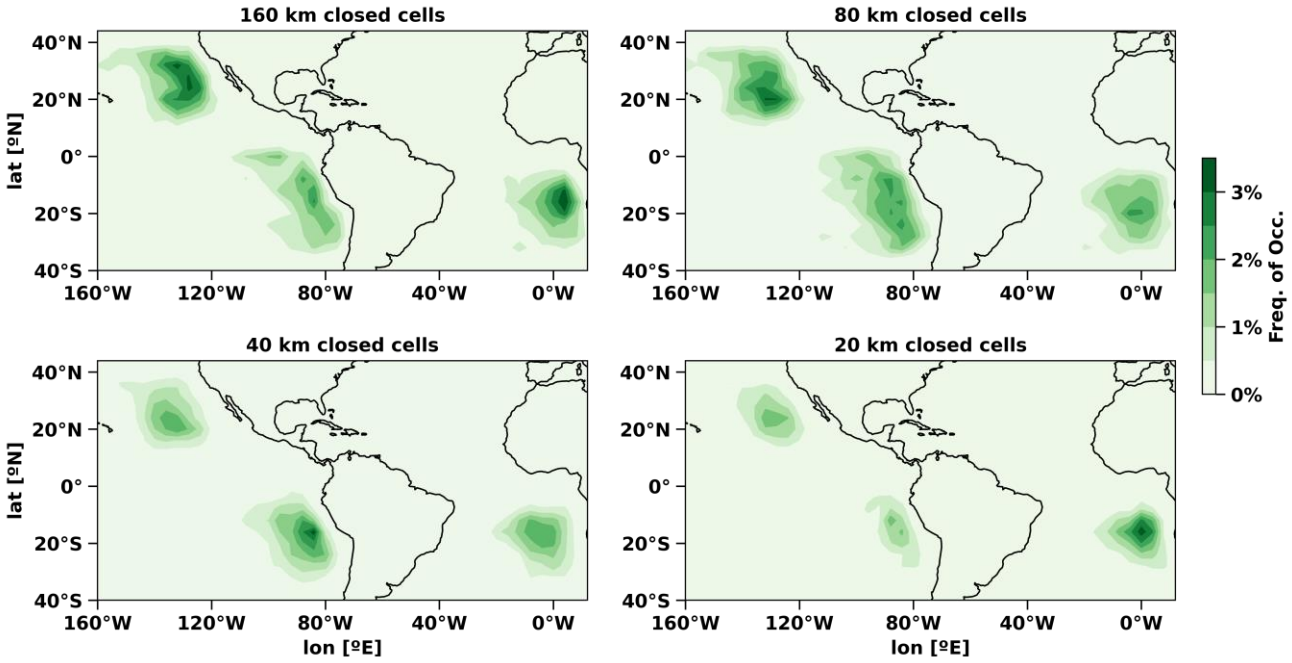

Fig. S1. Frequency of occurrence of closed cells at cell sizes of 160 km, 80 km, 40 km, and 20 km. Data is binned into boxes of 4º in longitude and latitude.

794 Figure S2

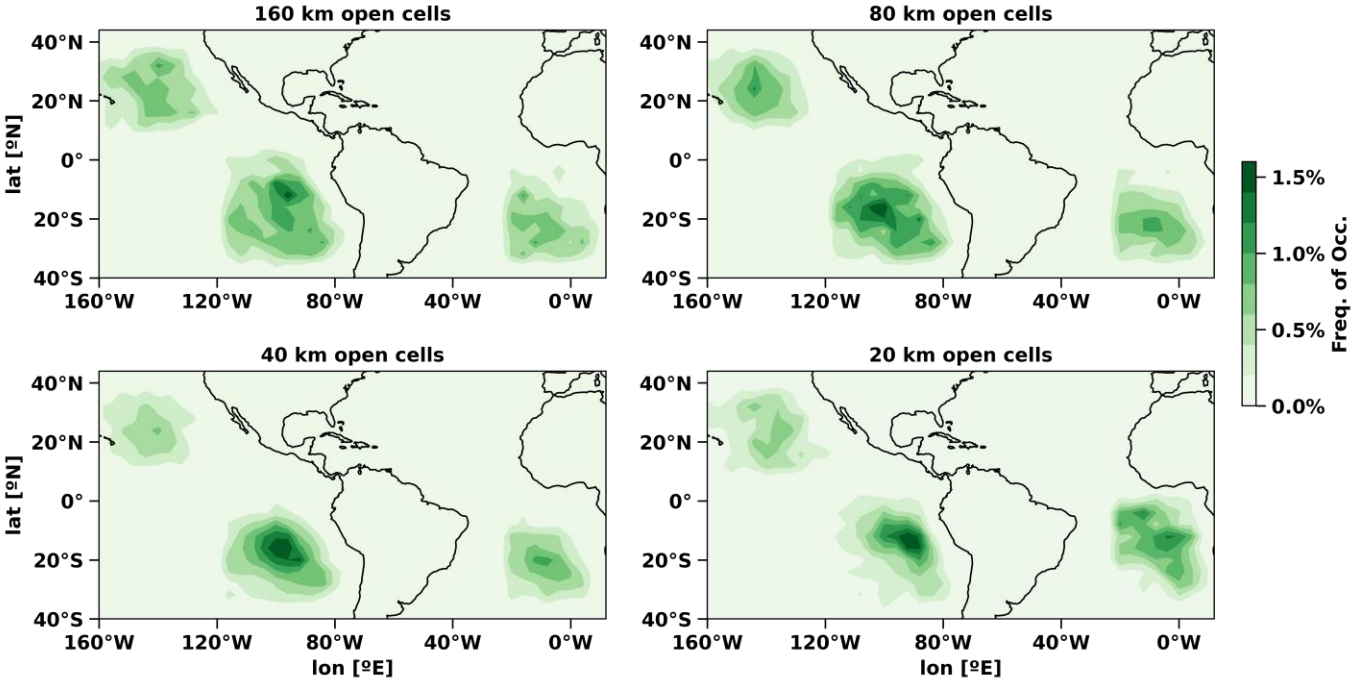

795

796 Fig. S2. Same as Fig. S1 but for open cells.

797

798